Simulation of the Quasi-Steady Behavior of Under-Expanded Supersonic Jets due to Instability Waves

Babak Emami[1], Markus Bussmann[1] and Honghi N. Tran[2]

[1] *Department of Mechanical and Industrial Engineering, University of Toronto, Toronto, ON, M5S 3G8, Canada*
[2] *Department of Chemical Engineering and Applied Chemistry, University of Toronto, Toronto, ON, M5S 3E5, Canada*

Email: *bemami@mie.utoronto.ca*

ABSTRACT

A time accurate numerical study was carried out to study the quasi-steady behavior of under-expanded jets. The quasi-steadiness is caused by interaction of the large scale instabilities with the shock cell structure of the under-expanded jet. A time marching TVD scheme along with a corrected $k-\varepsilon$ turbulence model, which accounts for compressibility and turbulence/shock wave interaction, was used for simulations. Then, linear instability theory was applied to the same jet to explain and support the numerical calculations. It was shown that the time dependent fluctuations in flow parameters were maximum in the vicinity of shock waves. In addition, two types of instability waves, corresponding to two distinct frequency ranges, were found to exist and interact with the flow structure.

1 BACKGROUND AND INTRODUCTION

The fouling of heat transfer surfaces in kraft recovery boilers is a significant concern for the pulp and paper industry. The usual approach to controlling fouling is the use of so-called "sootblowers," that utilize boiler steam to generate supersonic steam jets that are literally used to knock deposits off of the boiler tubes. Sootblower nozzles are nominally designed such that the steam is expanded to ambient pressure at the nozzle exit. But in reality, sootblower jets never perform at exactly the design condition, and so the jet pressure at the nozzle exit is never exactly the ambient pressure inside the boiler.

When the nozzle exit pressure of a supersonic jet is higher than the ambient pressure, shock and expansion waves form, the so-called multi-cell shock structure, through which the pressure of the flow field drops to the ambient value. These jets are usually referred to as "under-expanded". Figure 1 shows a Schlieren flow visualization of an under-expanded jet [1]. As can be seen, the shock cell structure consists of oblique shock waves, and it decays with distance from the nozzle exit due to the interaction with turbulence.

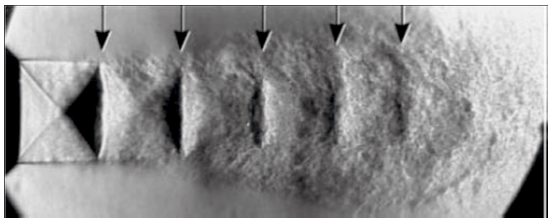

Figure 1: Flow visualization of an under-expanded jet by Panda [1]; the nozzle exit is on the left hand side.

The interaction of large scale flow instabilities with shock and expansion waves is one of the important physical phenomena of under-expanded jets. This interaction leads to time-dependent oscillating (quasi-steady) behavior of the flow field. This physical phenomenon is known and has been observed experimentally (e.g. Refs. [1, 2]). Although simulation of under-expanded jets is challenging, given the complicated interaction of shock waves and turbulent mixing, quasi-steady behavior of these flows seems to be captured well by the present simulations.

Here, time accurate simulations are used to study the quasi-unsteadiness of the under-expanded jet of Seiner and Norum [3], with an exit to ambient pressure ratio of 1.45 and an exit Mach number of 2.0, both in the time and frequency domains. The measurements of Seiner and Norum are frequently cited and used to assess numerical models (other measurements by Norum and Seiner [15], for a similar under-expanded jet, confirm the validity of this data). Then, linear jet in-

stability theory [4] is applied to the same jet, and the results are used to explain and support the numerical study. All of the simulations were 2-D axisymmetric, and so the azimuthal instability modes were not captured; given the fine meshes required to capture the shock wave phenomena, 3-D simulations were not attempted.

2 Existence of Instability Waves

The linear instability theory of Tam and Hu [4] for a round compressible jet is used to explain some of the numerical results of the present study. This theory is based on a solution of the linearized Euler equations. The linear solution to an axisymmetric jet yields relations for pressure perturbations inside and outside the jet, respectively, as

$$p_i = [H_0^{(1)}(i\eta_o D/2)J_0(\eta_i r)/J_0(\eta_i D/2)]\exp[i(\alpha x - \omega t)] \tag{1}$$

and

$$p_o = H_0^{(1)}(i\eta_o r)\exp[i(\alpha x - \omega t)] \tag{2}$$

where $H_0^{(1)}$ is the zeroth-order Hankel function of the first kind, J_0 is the zeroth-order Bessel function of the first kind, D is the nozzle exit diameter, α is the wave number, ω is frequency, and x, r and t are the axial and radial coordinates and time, respectively. Also, $\eta_o = (\alpha^2 - \omega^2/a_\infty^2)^{1/2}$ and $\eta_i = [(\omega - U_e\alpha)^2/a_e^2 - \alpha^2]^{1/2}$, where a_∞ is the ambient speed of sound, and a_e and U_e are the speed of sound and the flow velocity at the nozzle exit, respectively. Setting the inside and outside solutions equal to each other at the jet boundary, one obtains

$$DS(\omega,\alpha) \equiv \frac{i\eta_o}{\rho_\infty\omega^2}J_0(\eta_i D/2)H_0^{(1)\prime}(i\eta_o D/2) -$$

$$\frac{\eta_i}{\rho_e(\omega - U_e\alpha)^2}H_0^{(1)}(i\eta_o D/2)J_0'(\eta_i D/2) = 0 \tag{3}$$

where $DS(\omega,\alpha)$ is usually referred to as the dispersion function. Solutions of DS yield the possible frequencies, ω, for a given wave number, α. These are referred to as instability modes.

This instability theory was applied to the jet studied here, and the solutions of the dispersion function were plotted in the ω plane, as can be seen in Figure 2, where ω_r and ω_i represent the real and imaginary parts of ω respectively, and αD = 30. The blue and red lines represent the zeros of the real and imaginary parts of DS, respectively; the intersections are the solutions of DS, i.e. the instability modes. By looking at the pressure eigenfunctions, Tam and Hu [4] argued that these instability modes correspond to two different categories: the Kelvin-Helmholtz and acoustic waves, represented by filled boxes and circles, respectively. Carrying out the calculations for different values of α, including complex values, yielded similar results. These confirm the existence of instability modes in the jet flow and will prove useful, when the simulation results are studied in the frequency domain.

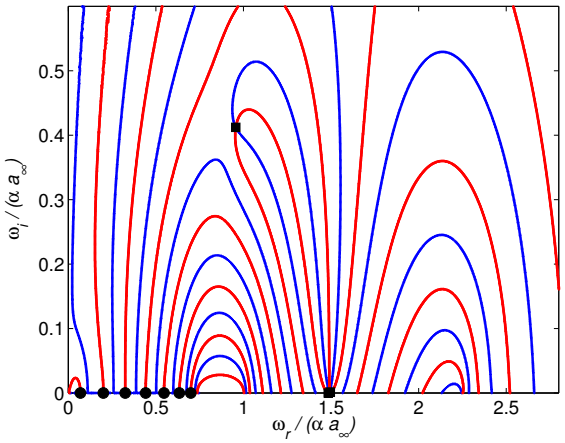

Figure 2: Solutions of the dispersion function, $DS(\omega,\alpha)$, in the ω plane, for αD = 30. Filled boxes and circles represent the Kelvin-Helmholtz and acoustic instability modes, respectively.

3 Numerical Method

CFDLib 3.02, a Computational Fluid Dynamics code developed at the Los Alamos National Laboratory, was used for calculations. To calculate the motion of a compressible flow, the Favre averaged equations of conservation of mass, momentum and energy must be solved,

$$\bar{\rho}\,\dot{\tilde{v}} = \frac{\partial \tilde{u}_i}{\partial x_i} \tag{4}$$

$$\bar{\rho}\,\dot{\tilde{u}}_i = -\frac{\partial \bar{p}}{\partial x_i} + \frac{\partial \bar{t}_{ij}}{\partial x_j} + \frac{\partial \lambda_{ij}}{\partial x_j} \tag{5}$$

$$\bar{\rho}\dot{\tilde{E}} = -\frac{\partial \bar{p}\tilde{u}_j}{\partial x_j} + \frac{\partial \tilde{u}_i \bar{t}_{ij}}{\partial x_j} + \tilde{u}_i\frac{\partial \lambda_{ij}}{\partial x_j} -$$

$$\frac{\partial q_{Lj} + q_{Tj}}{\partial x_j} + \bar{\rho}\varepsilon \tag{6}$$

along with an equation of state $\bar{p} = \bar{\rho} R \tilde{T}$, where ρ is density, v is specific volume, u_i is the velocity vector, x_i is the coordinate vector, p is pressure, t_{ij} is the molecular stress tensor, λ_{ij} is the Reynolds stress tensor, E is specific total energy, q_{Lj} and q_{Tj} are the laminar and turbulent heat flux vectors, respectively, ε is the turbulence dissipation rate, T is temperature, and '$\bar{}$', '$\tilde{}$' and '$\dot{}$' represent the Reynolds average, Favre average and Lagrangian derivative, respectively.

The turbulence model is the standard $k-\varepsilon$ model, with modifications applied to account for the effects of structural compressibility [5], realizability [6], and shock unsteadiness [7]. The turbulence kinetic energy k and dissipation ε equations are [8]

$$\bar{\rho}\dot{k} = \lambda_{ij}\frac{\partial \tilde{u}_i}{\partial x_j} - \bar{\rho}\varepsilon + \frac{\partial}{\partial x_j}[(\mu + \frac{\mu_T}{\sigma_k})\frac{\partial k}{\partial x_j}] \tag{7}$$

$$\bar{\rho}\dot{\varepsilon} = C_{\varepsilon 1}\frac{\varepsilon}{k}\lambda_{ij}\frac{\partial \tilde{u}_i}{\partial x_j} - C_{\varepsilon 2}\bar{\rho}\frac{\varepsilon^2}{k} + \frac{\partial}{\partial x_j}[(\mu + \frac{\mu_T}{\sigma_\varepsilon})\frac{\partial \varepsilon}{\partial x_j}] \tag{8}$$

where $C_{\varepsilon 1}$ (=1.44), $C_{\varepsilon 2}$ (=1.92), σ_k (=1.0) and σ_ε (=1.3) are constant closure coefficients, and from the dynamic eddy viscosity $\mu_T = C_\mu \bar{\rho}\frac{k^2}{\varepsilon}$, C_μ is an additional coefficient.

To account for the structural compressibility, Heinz [5] suggested that

$$C_\mu = 0.07\exp(-0.4M_g) \tag{9}$$

where M_g ($=\frac{S_g l_g}{a}$) is the gradient Mach number, and characterizes the strength of compressibility [9]; $S_g = \frac{\partial U_1}{\partial x_2}$ is the mean shear rate, U_1 and x_2 are the streamwise mean velocity and the shear direction coordinate, respectively, l_g is the correlation length of the streamwise fluctuating velocities in the shear direction, and a is the local sound speed. Tandra et al. [10] suggested that l_g be calculated as $l_g = C_D\frac{k^{3/2}}{\varepsilon}$, where C_D is a closure coefficient usually considered to be 0.09.

To ensure the positivity of the turbulence kinetic energy in the vicinity of shock waves, Thivet et al. [6] suggested a realizability condition on the eddy viscosity,

$$\mu_T = \bar{\rho}\min(C_\mu\frac{k^2}{\varepsilon}, \sqrt{C_\mu}\frac{k}{S_{Thivet}}) \tag{10}$$

where S_{Thivet} is defined as

$$S_{Thivet} = \sqrt{2(S_{ij}S_{ji} - \frac{1}{3}S_{kk}^2)} \tag{11}$$

where S_{ji} is the strain tensor.

Finally, to account for shock unsteadiness effects, unsteady motion of the shock wave front caused by the turbulence scale fluctuations, Sinha et al. [7] proposed that the turbulence production term, P_k, be calculated as

$$P_k = c_\mu^{'}\mu_T(2S_{ij}S_{ji} - \frac{2}{3}S_{kk}^2) - \frac{2}{3}\bar{\rho}kS_{kk} \tag{12}$$

where

$$c_\mu^{'} = 1 - f_s[1 + \frac{1}{\sqrt{3}}\frac{b_1^{'}\varepsilon}{kS_{Thivet}C_\mu}] \tag{13}$$

and

$$f_s = \frac{1}{2} - \frac{1}{2}\tanh(5\frac{S_{kk}}{S_{Thivet}} + 3) \tag{14}$$

and S_{Thivet} is defined by Equation 11. Equation 14 defines f_s such that f_s is close to 1 in highly compressed regions and close to 0 otherwise.

The original version of CFDLib included an implementation of the standard $k-\varepsilon$ model. The compressibility modifications were implemented by Tandra [11], while the other two were implemented by Emami et al. [12].

The numerical scheme implemented in CFDLib is a finite volume, explicit, cell-centered, total variable diminishing (TVD) method, that utilizes an arbitrary Lagrangian-Eulerian (ALE) time split operator for advancing the averaged flow variables. For details of the turbulence model and numerical method, refer to Ref. [12].

4 RESULTS

All simulations were run in a 2-D axisymmetric coordinate system. Based on the pressure ratio values, the inlet boundary conditions (velocity, density and temperature) corresponding to the nozzle exit were calculated. The ambient pressure was applied as a boundary condition far from the jet centerline. The calculations were performed on different computational domains and using different meshes, to assess both domain size and mesh dependence. Simulations were run from t=0 to t=20 msec. After about 4 msec the jet flow reached a quasi-steady form, but as expected, the time dependent oscillations in flow parameters were not damped. Data

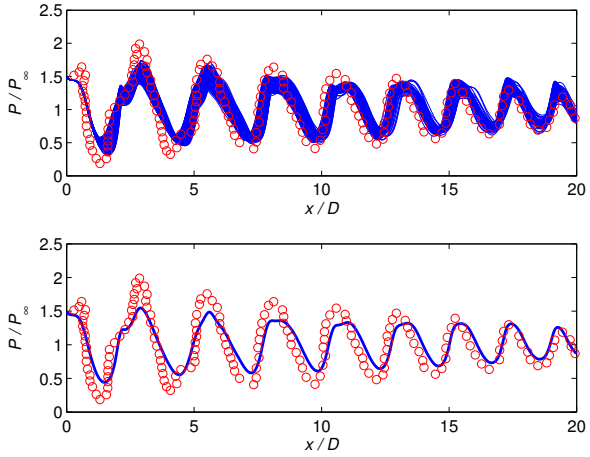

Figure 3: Distribution of instantaneous pressure at dif ferent times (top), and time average pressure (bottom along the jet centerline. The circles show the measurements of Seiner and Norum [3].

files were dumped every 2×10^{-4} sec, i.e. the "sampling" frequency was $1/(2 \times 10^{-4})$ Hz. Using higher sampling frequencies did not yield significantly different results.

Figure 3 (top) shows instantaneous pressure along the centerline of the jet, corresponding to 80 different times from 4 msec to 20 msec. As can be seen, for the first diameter away from the nozzle exit, the pressur does not fluctuate; this is in agreement with the mea surements of Panda [1], that indicated the shock cel closest to the nozzle exit does not oscillate. Furthe downstream, the value of pressure at each point fluc tuates with time and the thin lines, related to instan taneous pressure, form one thick line. Figure 3 (bot tom) shows the time average pressure along the cen terline. As shown in Figure 3, overall agreement of th simulation results with the data set of Seiner and No rum [3] is satisfactory. The discrepancies, especially i the pressure wave amplitudes, may be due to both ex perimental errors (especially given the unsteady natur of the flow), and the inability of RANS simulations t capture some of the physical phenomena of the flow Similar disagreements have been reported by other researchers (e.g. [13] and [14]).

To show that the fluctuations are not limited to the centerline and occur throughout the flow field, the instantaneous and time average pressures along $r/D = 0.25$ and $r/D = 0.45$ lines are plotted in Figures 4 and 5, respectively; note that the experimental data shown in these two figures are those of Norum and Seiner [15].

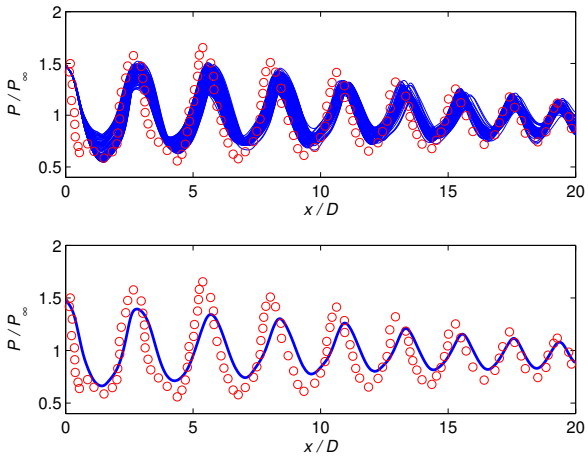

Figure 4: Distribution of instantaneous pressure at different times (top), and time average pressure (bottom) along $r/D = 0.25$. The circles show the measurements of Norum and Seiner [15].

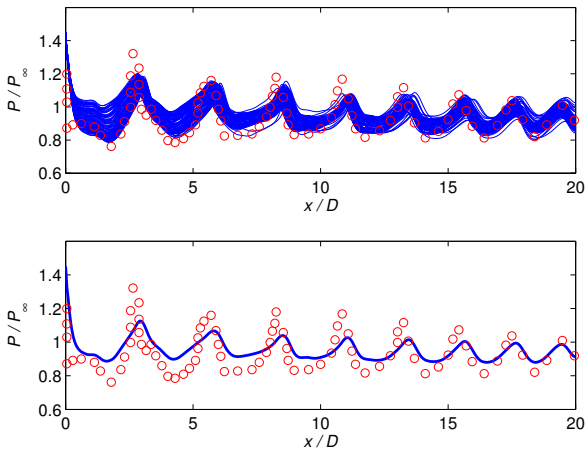

Figure 5: Distribution of instantaneous pressure at different times (top), and time average pressure (bottom) along $r/D = 0.45$. The circles show the measurements of Norum and Seiner [15].

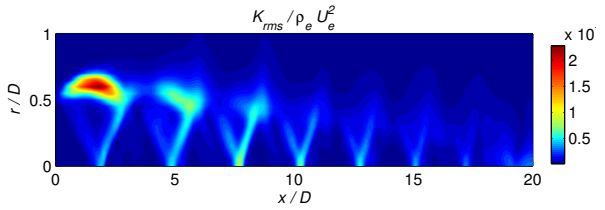

Figure 6: Instability wave kinetic energy contours

To better assess these fluctuations in the time domai it is useful to look at the root mean squared (*rms*) values of the flow parameters. We define a kinetic energy related to fluctuations of the flow parameters, K_{rms},

$$K_{rms} = \frac{1}{2}\rho_M(u^2_{x,rms} + u^2_{r,rms}) \qquad (15)$$

where ρ_M is the time average density, and $u_{x,rms}$ and $u_{r,rms}$ are the *rms* values of axial and radial flow velocities, respectively. We refer to this as the "instability wave kinetic energy", since the fluctuations are caused by the flow instabilities.

Figure 6 shows contours of the instability wave kinetic energy, obtained from simulation. The maximum kinetic energy occurs at the jet boundary close to the nozzle exit; see the red color in the contour. This should be related to Kelvin-Helmholtz instabilities, as they occur at the boundary of the jet with the ambient fluid. In the rest of the plot, the higher kinetic energies can be seen as oblique lines. These are the oblique shock waves formed in the under-expanded jet, and indicate that the maximum fluctuations occur in the vicinity of shocks. Studying the pressure contours confirms this finding, indicating that the fluctuations result from the interaction of instability waves and shock waves: Figure 7 (top) shows the time average pressure, P_M, contours, and Figure 7 (bottom) shows the *rms* pressure, P_{rms}, contours, normalized by the ambient pressure, P_∞. The vertical dashed lines show the locations at which P_{rms} is maximum; as can be seen, the maximum P_{rms} correspond to the points between the compression and expansion regions, where the shock waves form. This, again, confirms that the maximum fluctuations occur in the vicinity of the shock waves.

The time dependent fluctuations can be transferred to the frequency domain using a Fourier transform. Figure 8 shows the same time average pressure contour (top), and the dominant Fourier transform of pressure (middle) and axial velocity (bottom) fluctuations along the jet centerline. It can be seen that the dominant Fourier transforms occur where the shock waves form, i.e. in front of the compression regions. This, again, confirms that the maximum fluctuations occur close to

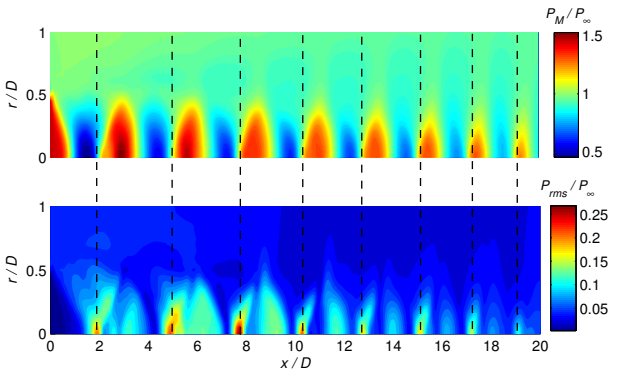

Figure 7: Time average (top) and rms (bottom) pressure contours; the vertical dashed lines show the locations at which P_{rms} is maximum.

shock waves.

Finally, Figure 9 shows the Fourier transform of pressure fluctuation at one point in the physical domain (x/D=5, r/D=0.5), versus frequency. As can be seen, the dominant Fourier transforms correspond to two distinct frequency ranges. These two distinct frequency ranges may be related to two instabilities: Kelvin-Helmholtz, and acoustic instability waves. These results are qualitatively in agreement with the results of the linear instability theory. Studying the spectrum at other points in the physical domain yielded similar results.

Future work includes filtering these dominant frequencies (one at a time, as illustrated in Figure 10), and then transferring the results back to the time domain, to confirm that the two dominant frequency ranges are related to the Kelvin-Helmholtz and acoustic instability waves.

REFERENCES

[1] J. Panda. Shock oscillation in under-expanded screeching jets. *J. Fluid Mech.*, 363:173-198, 1998.

[2] J. Panda and R.G. Seasholtz. Measurement of shock structure and shock-vortex interaction in under-expanded jets using Rayleigh scattering. *Phy. Fluids*, 11(12):3761-3777, 1999.

[3] J.M. Seiner and T.D. Norum. Aerodynamic aspects of shock containing jet plumes. *AIAA Paper 80-0965*, 1980.

[4] C.K.W. Tam and F.Q. Hu. On the three families of instability waves of high speed jets. *J. Fluid Mech.*, 210:447-483, 1989.

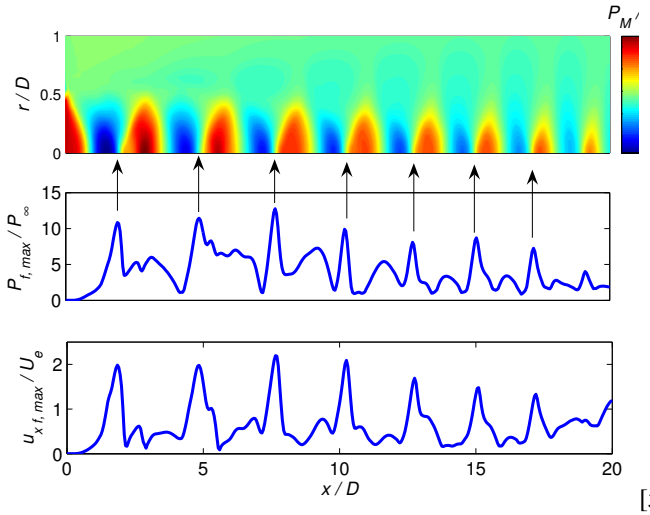

Figure 8: Time average pressure contour (top), and distribution of the dominant Fourier transform of pressure (middle) and axial velocity (bottom) along the jet centerline.

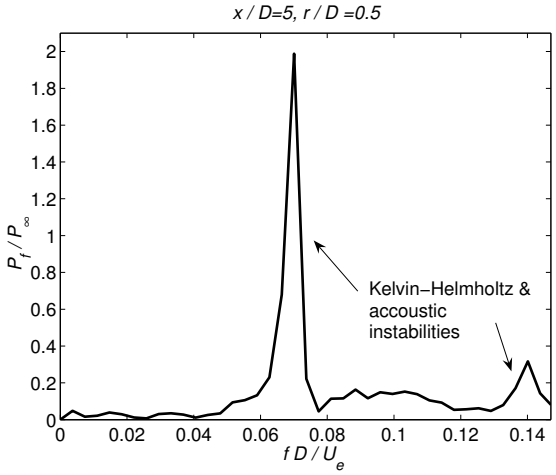

Figure 9: Pressure fluctuations in the frequency domain: Fourier transform at x/D=5, r/D=0.5.

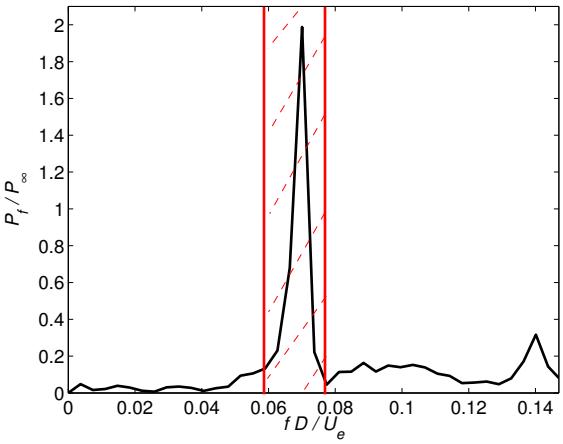

Figure 10: Filtration of the pressure spectrum.

[5] S. Heinz. A model for the reduction of the turbulent energy redistribution by compressibility. *Phy. Fluids*, 15(11):3580-3583, 2003.

[6] F. Thivet, D.D. Knight, and A.A. Zheltovodov. Importance of limiting the turbulent stresses to predict 3-D shock wave/boundary layer interactions. *23rd Symposium on Shock Waves, Paper No. 2761*, 2001.

[7] K. Sinha, K. Mahesh, and G.V. Candler. Modeling the effect of shock unsteadiness in shock/turbulent boundary-layer interactions. *AIAA Journal*: 43(3):586-594, 2005.

[8] D.C. Wilcox. Turbulence modeling for CFD. *DCW Industries*, 2004.

[9] S. Sarkar. The stabilizing effect of compressibility in turbulent shear flow. *Journal of Fluid Mechanics*, 282:163-186, 1995.

[10] D.S. Tandra, A. Kaliazine, and D.E. Cormack. Numerical simulation of supersonic jet flow using a modified $k-\varepsilon$ model. *International Journal of Computational Fluid Dynamics*, 20(1):19-27, 2006.

[11] D. Tandra. Development and application of a turbulence model for a sootblower jet propagating between recovery boiler superheater platens. *PhD Thesis, University of Toronto*, 2005.

[12] B. Emami, M. Bussmann, and H.N. Tran. T urbulence/shock wave interaction in simulation of under-expanded supersonic jets. *16th Annual Conference of the CFD Society of Canada*, 2008.

[13] P.S. Cumber, M. Fairweather, and S.A.E.G. Falle. Predictions of the structure of turbulent, moderately underexpanded jets. *Journal of Fluids Engineering, Transactions of the ASME*, 116(4):707-713, 1994.

[14] S.M. Dash, D.E. Wolf, and J.M. Seiner. Analysis of turbulent underexpanded jets, Part I: Parabolized Navier-Stokes model, SCIPVIS. *AIAA Journal*, 23(4):505-514, 1985.

[15] T.D. Norum and J.M. Seiner. Measurements of mean static pressure and far-field acoustics of shock-containing supersonic jets. *NASA Technical Memorandum 84521*, 1982.